3D Tunable, Multiscale, and Multistable Vibrational Micro-Platforms Assembled by Compressive Buckling

Xin Ning, Heling Wang, Xinge Yu, Julio A. N. T. Soares, Zheng Yan, Kewang Nan, Gabriel Velarde, Yeguang Xue, Rujie Sun, Qiyi Dong, Haiwen Luan, Chan Mi Lee, Aditya Chempakasseril, Mengdi Han, Yiqi Wang, Luming Li, Yonggang Huang, Yihui Zhang, and John A. Rogers**

Microelectromechanical systems remain an area of significant interest in fundamental and applied research due to their wide ranging applications. Most device designs, however, are largely 2D and constrained to only a few simple geometries. Achieving tunable resonant frequencies or broad operational bandwidths requires complex components and/or fabrication processes. The work presented here reports unusual classes of 3D micromechanical systems in the form of vibratory platforms assembled by controlled compressive buckling. Such 3D structures can be fabricated across a broad range of length scales and from various materials, including soft polymers, monocrystalline silicon, and their composites, resulting in a wide scope of achievable resonant frequencies and mechanical behaviors. Platforms designed with multistable mechanical responses and vibrationally decoupled constituent elements offer improved bandwidth and frequency tunability. Furthermore, the resonant frequencies can be controlled through deformations of an underlying elastomeric substrate. Systematic experimental and computational studies include structures with diverse geometries, ranging from tables, cages, rings, ring-crosses, ring-disks, two-floor ribbons, flowers, umbrellas, triple-cantilever platforms, and asymmetric circular helices, to multilayer constructions. These ideas form the foundations for engineering designs that complement those supported by conventional, micro-electromechanical systems, with capabilities that could be useful in systems for biosensing, energy harvesting, and others.

Dr. X. Ning, Dr. X. Yu, Dr. J. A. N. T. Soares, Dr. Z. Yan, K. Nan, G. Velarde, Y. Wang
Department of Materials Science and Engineering
Frederick Seitz Materials Research Laboratory
University of Illinois at Urbana-Champaign
Urbana, IL 61801, USA

Dr. H. Wang, Y. Xue, H. Luan, Prof. Y. Huang
Department of Civil and Environmental Engineering, and Department of Mechanical Engineering
Northwestern University
Evanston, IL 60208, USA

R. Sun
Advanced Composites Centre for Innovation and Science
University of Bristol
Bristol BS8 1TR, UK

Q. Dong
Department of Industrial and Enterprise Systems Engineering
University of Illinois at Urbana-Champaign
Urbana, IL 61801, USA

C. M. Lee
Department of Chemistry
University of Illinois at Urbana-Champaign
Urbana, IL 61801, USA

A. Chempakasseril
Department of Chemical and Biomolecular Engineering
University of Illinois at Urbana-Champaign
Urbana, IL 61801, USA

DOI: 10.1002/adfm.201605914

M. Han
National Key Laboratory of Science and Technology on Micro/Nano Fabrication
Peking University
Beijing 100871, P. R. China

Prof. L. Li
Department of Aeronautics and Astronautics Engineering
School of Aerospace Engineering
Man-machine-Environment Engineering Institute
Tsinghua University
Beijing 100084, P. R. China

Prof. Y. Zhang
Department of Engineering Mechanics
Center for Mechanics and Materials
AML
Tsinghua University
Beijing 100084, P. R. China
E-mail: yihuizhang@tsinghua.edu.cn

Prof. J. A. Rogers
Department of Materials Science and Engineering
Department of Biomedical Engineering
Department of Neurological Surgery
Department of Chemistry
Department of Mechanical Engineering
Department of Electrical Engineering, and Department of Computer Science
Simpson Querrey Institute, Feinberg Medical School
Center for Bio-Integrated Electronics
Northwestern University
Evanston, IL 60208, USA
E-mail: jrogers@northwestern.edu

1. Introduction

Micro-electromechanical systems (MEMS) exploit structural vibrations for precision mass sensing,[1–3] microscale rheology,[4–7] measurement of cell mechanics,[8–12] energy harvesting[13–15] and other important purposes. Current MEMS devices are limited to only a few, largely 2D geometries such as cantilevered beams,[16–18] doubly clamped bridges,[19] stressed wires,[20] and other constructs based on flat membranes and plates.[7,21] These devices also, by consequence, operate in a largely simple, 2D manner, thereby limiting their utility when full, 3D motions are required. For example, biological cells[22–25] and tissues[26–29] have anisotropic mechanical properties. Investigating the mechanical properties of these materials demands devices with capabilities for operation in 3D space. In addition, ambient vibrations are essentially 3D, and hence conventional 2D MEMS devices for kinetic energy harvesting applications have disadvantages.

Recent advances in MEMS technologies include the development of devices with resonant frequencies that can be tuned to compensate for frequency shifts associated with changes in the operating environment[20,30–32] and that can be continuously adapted for time-varying ambient vibrations, both of which improve the efficiency for energy harvesting. Common methods for tuning the frequency include changing the associated mass and/or tuning the effective stiffness of the resonator by applying stresses through piezoelectric effects, thermal expansion, or electrostatic forces.[20,30–32] These approaches require, however, integration of additional components and materials, and, therefore, significantly complicate the fabrication process. 3D structures formed via origami,[33,34] buckling,[35–38] and 3D printing[39] have attracted significant attentions due to their wide range of applications such as microphysiological systems,[39] cell studies,[40,41] biomimic actuators,[42,43] and the control of wave propagation.[44,45] However, their applications in MEMS resonators and energy harvesters remain to be fully explored.

This paper presents a systematic set of experimental and theoretical studies of a broad set of 3D vibrational structures with diverse geometries, assembled by controlled compressive buckling from advanced materials including soft polymers, brittle silicon, and their composites, with potential use as 3D MEMS resonators and kinetic energy harvesters. These platforms offer resonant frequencies that can be tuned by varying the in- and out-of-plane sizes and compositions of the structures or by inducing deformations in the underlying elastomeric substrates. Multistable structures provide routes to increase the bandwidth and tunability. Demonstrations include a broad set of 3D architectures ranging from tables, cages, rings, ring-disks, ring-crosses, flowers, umbrellas, membrane-cantilever hybrid structures, asymmetric circular helices, to multilayer cage structures.

2. Results and Discussion

Cage and table structures serve as examples to demonstrate the essential physics that underpins the dependence of resonant vibrational frequencies on compressive strains applied on the structures via deformations of the substrate (**Figure 1**). Fabrication follows previously reported approaches in deterministic mechanical assembly.[46–49] Specifically, a set of microfabrication processing steps first produces a collection of 2D precursor structures. Transfer onto a prestretched elastomeric substrate after treating the contacting surfaces to define a collection of sites for strong mechanical bonding prepares the system for geometrical transformation into a 3D structure. Here, relaxing the stretch in the substrate imposes compressive forces on the 2D precursors at the bonding sites, and leads to delamination and consequent out-of-plane translational and rotational motions of the nonbonded regions. The Experimental Section describes the details. Here, the resulting 3D structures serve as vibrational platforms on elastomeric substrates. Controlling the deformation of the latter offers a means for adjusting the 3D geometries and, by consequence, the resonant frequencies.

Figure 1a,b presents scanning electron microscope (SEM) images and results of 3D finite element analyses (FEA) for the cage and table structures compressed at 20%, 30%, and 40% biaxial strains (denoted as $\varepsilon_{\text{comp}}$). The values of $\varepsilon_{\text{comp}}$ correspond to the magnitude of strain released from the substrate initially in its prestretched state. Each structure consists of a patterned layer of a photodefinable polymer (SU8, MicroChem) with thickness of 10 µm, and width of 200 µm (table) and 50 µm (cage) for the support features. Figure S1 (Supporting Information) presents detailed geometries for the 2D precursors in both cases. Figure 1a,b shows that, as the compressive strains increase, the in-plane sizes of the cage and table structures decrease and heights increase, as expected. The resulting geometries, in all cases, show good agreement with the FEA. Figure 1c,d illustrates two representative vibrational modes, left-right and back-front modes, obtained by FEA. Here, the images in green and gray correspond to the shapes of the 3D structure at two utmost phases (denoted by phases 0° and 180°) during harmonic motions. Due to the thin geometries of the features, cooperative deformations of different components occur mainly by bending and twisting.

A system that captures the time dependence of laser light scattered from the vibrating structures yields frequencies and amplitudes associated with the motions. Figure 1e,f presents the measured amplitude-frequency responses of the cage structures in Figure 1a,b for the left-right and back-front modes. Although the amplitudes depend linearly on the intensity of the scattered laser light for a given experimental configuration, comparisons between different structures are difficult due to variations in geometry and baseline values of scattered light. As a result, Figure 1e,f presents the amplitudes normalized by the value at resonance, to facilitate comparisons. The Experimental Section describes the details of the measurement system and method.

The results in Figure 1e,f show that resonant frequencies decrease as the compressive strains increase, confirming the tunability by substrate deformation mentioned previously. As a comparison, Figure 1g shows corresponding FEA results. Due to the fourfold rotational symmetry of these two structures, the left-right and the back-front modes have the same amplitude-frequency responses in FEA. Figure 1h summarizes the values of resonant frequencies obtained from experiments and FEA. For the left-right mode, the measured resonant frequency reduces from 6.45 and 5.85 to 5 kHz when the compressive strain increases from 20% and 30% to 40%, respectively. The resonant frequencies for the back-front mode are 6.4, 5.95, and 5 kHz for 20%, 30%, and 40% biaxial

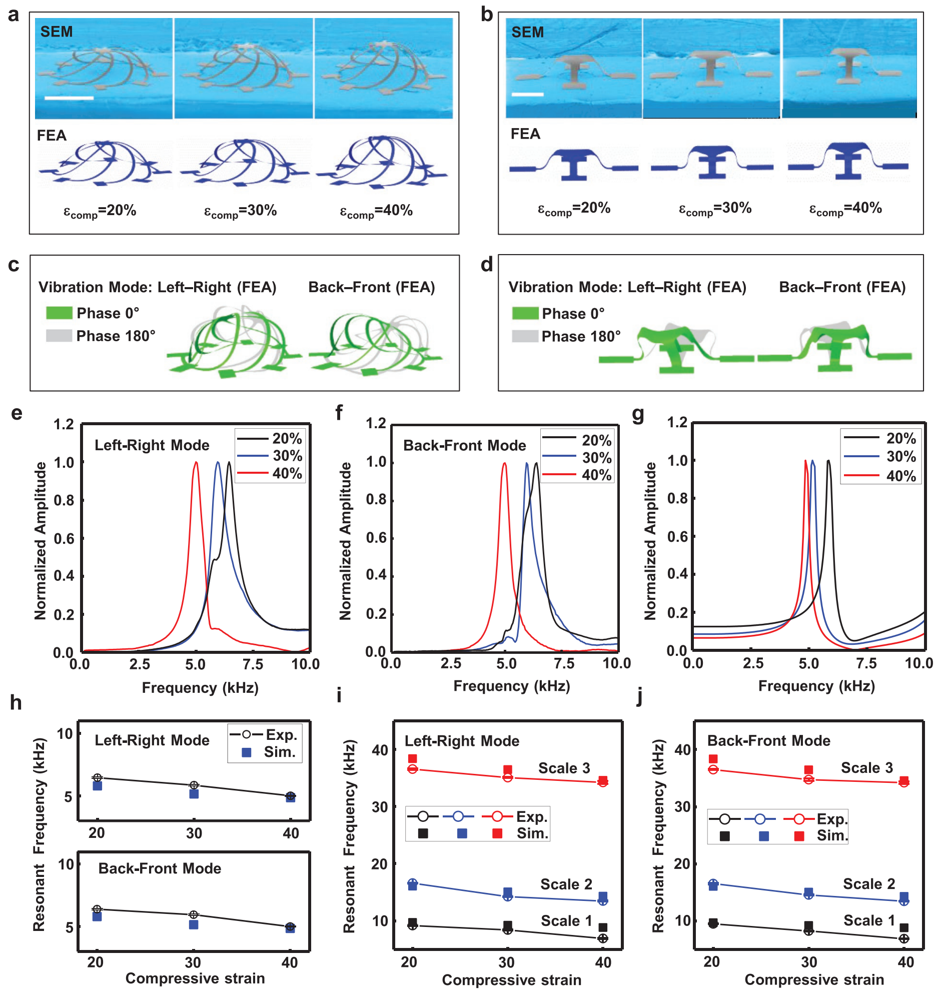

Figure 1. Resonant vibrational frequencies of 3D structures and their dependence on compressive strains applied during assembly by controlled buckling. a) SEM images and FEA results for 3D cage structures buckled at three strain levels. Scale bar: 1 mm. b) SEM images and FEA results of table structures buckled at three strain levels. Scale bar: 500 µm. c,d) FEA results for the vibration modes of cage and table structures, respectively, in which the amplitudes are magnified to clearly illustrate the modes. e,f) Measured amplitude-frequency responses of left-right and back-front vibrational modes, respectively, for cage structures. g) Simulated amplitude-frequency responses of left-right and back-front vibration modes by FEA. h) Comparison between measured and simulated resonant frequencies for cage structures. i,j) Measured and simulated resonant frequencies of left-right and back-front vibrational modes, respectively, at three strain levels and 3D scales for table structures.

compressive strains, respectively. The FEA results confirm the monotonically decreasing relation between resonant frequencies and compressive strains. Figure S1 (Supporting Information) presents the vibrational modes and resonant frequencies of the up-down mode corresponding to 20%, 30%, and 40% biaxial compressive strains. The dependence of the resonant frequency on the compressive strain can be mainly attributed to changes in the shapes of the 3D structures. In general, the resonant frequency (f) relates to the effective stiffness (K) and effective mass (M) of a vibrational system by $f = \sqrt{K/M}$, where K and M are dependent on the shape, material properties, and the vibrational mode of the 3D structure. The shapes of the 3D structures change significantly with compressive strain, thereby inducing changes in the resonant frequency, but without significantly affecting the nature of the vibrational mode.

Figure 1i,j shows experimental and FEA resonant frequencies of table structures at 20%, 30%, and 40% biaxial compressive strains and three length scales (denoted as scales 1, 2, and 3). The in-plane size and thickness of the 2D precursor for scale 3 are 800 and 4 µm, respectively. The in-plane sizes of scales 1 and 2 structures are three and two times of the scale 3 structures, and their thicknesses are 10 and 7 µm, respectively. Figure S1b (Supporting Information) shows SEM images of the three structures at the same strain, demonstrating their nearly identical overall shapes. At each scale, the resonant frequencies decrease with increasing compressive strains. At each compressive strain, the resonant frequencies increase as the dimensions decrease. The FEA results show good quantitative agreement with experimental measurements. The conclusion is that a wide range of resonant frequencies can be achieved by varying the compressive strains or scaling the dimensions without changing shape.

The resonant frequencies also depend on material composition and structural dimensions (**Figure 2**). Cage structures serve as examples to demonstrate sensitivity to composition.

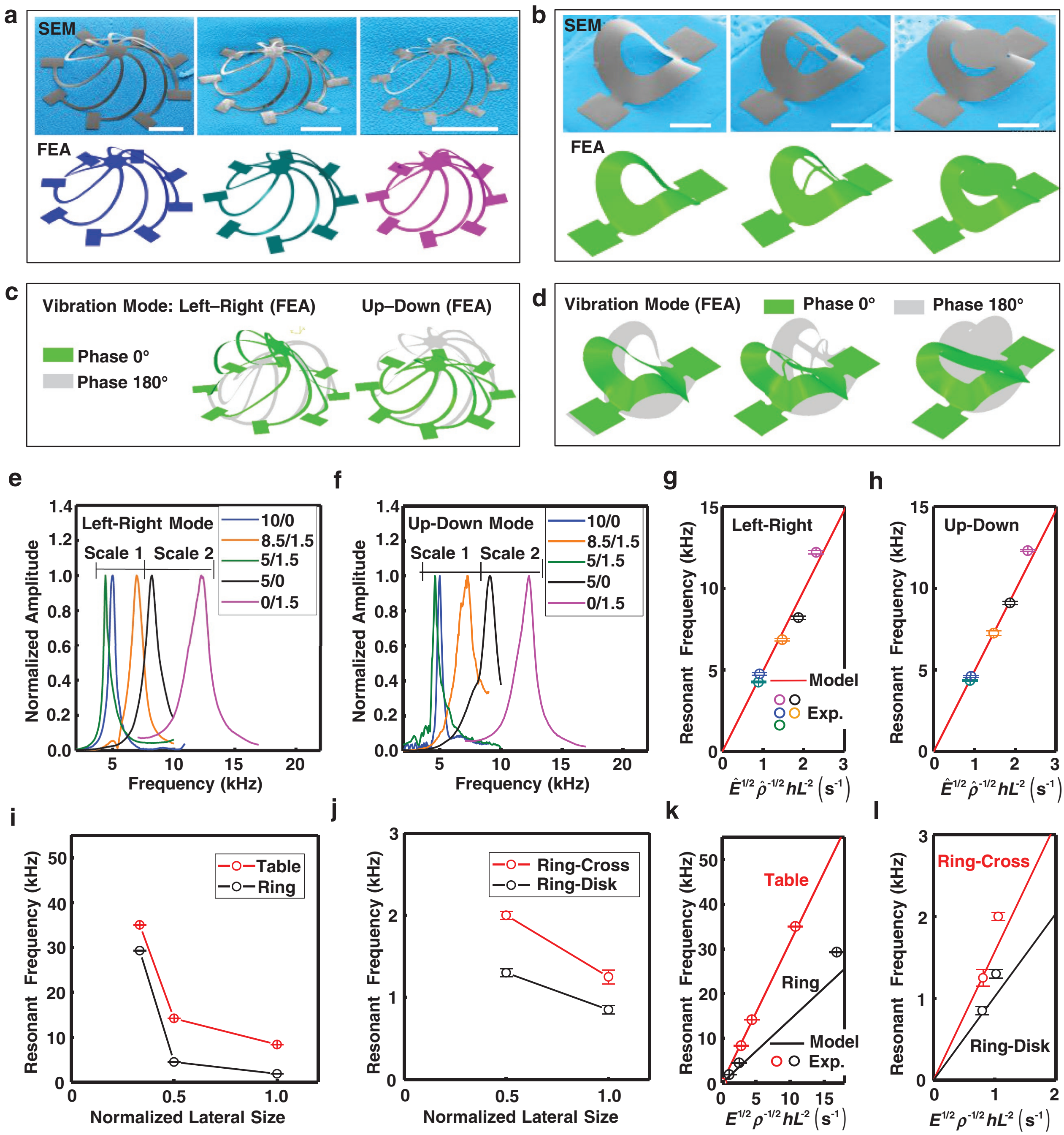

Figure 2. Resonant frequencies of 3D structures as a function of material composition and dimensional scale. a) SEM images and FEA results for cage structures comprised of SU8, Si-SU8 composite, and Si. Scale bars: 500 µm. b) SEM images and FEA results for ring, ring-cross, and ring-disk structures. Scale bars: 1 mm. c,d) FEA images of the vibrational modes, in which the amplitudes are magnified to clearly illustrate the modes. e,f) Measured amplitude-frequency responses of left-right and back-front vibrational modes, respectively, for various combinations of SU8 and Si thicknesses. The legends represent the thickness ratios between SU8 and Si (unit: µm). g,h) Experimental results compared with the scaling law for the resonant frequencies for SU8, Si, and SU8/Si cage structures. i) Measured resonant frequencies of left-right vibrational modes for table and ring structures at three scales. j) Measured resonant frequencies of left-right vibrational modes for ring-cross and ring-disk structures at two scales. k) Experimental results compared with the scaling law for the resonant frequencies of table and ring structures. l) Experimental results compared with the scaling law for the resonant frequencies of ring-cross and ring-disk structures.

Figure 2a presents SEM images and FEA results of three representative cage structures made of a single layer of SU8, a bilayer of SU8 and monocrystalline Si, and a single layer of monocrystalline Si (left to right). Figure 2c shows two representative vibrational modes, left-right and up-down modes, obtained by FEA. Figure 2e,f presents the measured amplitude-frequency responses of these modes. Results in Figure 2e,f include three cage structures (denoted as scale 1 in Figure 2e,f) constructed of SU8 (10 µm), SU8 (8.5 µm)/silicon (1.5 µm), and SU8 (5 µm)/Si (1.5 µm), and two cage structures whose in-plane sizes are a factor of two smaller than those at scale 1. Because the modulus (130 GPa) of Si is much larger than that (4.02 GPa) of SU8, the 3D cage structure made of SU8 (8.5 µm)/Si (1.5 µm) has a much higher resonant frequency than that of the SU8 (10 µm), even though both the lateral sizes and the total thicknesses are the same. The resonant frequencies of the smaller cage structures (scale 2, i.e., half the size of scale 1 cages) are higher than all three of the scale 1 cage structures. The 3D cage of Si (1.5 µm) has higher resonant frequencies than those of the SU8 (5 µm), because the effect of the modulus overcomes that of the thickness in this case.

A scaling law provides quantitative understanding of the effect of material and geometrical parameters on the resonant frequency. For a vibrational mode dominated by bending, the effective stiffness (K) of the 3D structure is proportional to $\hat{E}h^3/L^2$, where $\hat{E}$ is the equivalent modulus, h the total thickness, and L the lateral size; the effective mass (M) is proportional to $\hat{\rho}hL^2$, with $\hat{\rho}$ being the equivalent density. Therefore, the resonant frequency can be written as

$$f = \alpha (K/M)^{1/2} = \alpha \hat{E}^{1/2} \hat{\rho}^{-1/2} h L^{-2} \tag{1}$$

where α is a dimensionless factor that depends on the shape of the 3D structure and the vibrational mode and can be determined from FEA. For a bilayer composite of SU8 and Si, the expressions for $\hat{E}$ and $\hat{\rho}$ are

$$\hat{E} = \frac{E_{SU8}^2 h_{SU8}^4 + 4E_{SU8}E_{Si}h_{SU8}^3 h_{Si} + 6E_{SU8}E_{Si}h_{SU8}^2 h_{Si}^2 + 4E_{SU8}E_{Si}h_{SU8}h_{Si}^3 + E_{Si}^2 h_{Si}^4}{(E_{SU8}h_{SU8} + E_{Si}h_{Si})(h_{SU8} + h_{Si})^3} \tag{2}$$

and

$$\hat{\rho} = \frac{\rho_{SU8}h_{SU8} + \rho_{Si}h_{Si}}{h_{SU8} + h_{Si}} \tag{3}$$

where E_{SU8}, E_{Si}, ρ_{SU8}, ρ_{Si}, h_{SU8}, and h_{Si} are the Young's modulus, density, and thickness of SU8 and Si, respectively. This scaling law matches the experiment results in Figure 2g,h and the FEA results in Figure S3 (Supporting Information) for a wide range of parameters.

Studies of three structures (ring, ring-cross, and ring-disk structure) demonstrate the relationship between the resonant frequencies and the length scales (Figure 2b). Figure 2b presents SEM images and FEA results. The vibrational direction lies along the two bonding sites. Figure 2d presents their vibrational modes. Figure 2i shows the resonant frequencies of the ring and table structures, plotted against their lateral sizes normalized by the largest scale. The results illustrate that the resonant frequencies increase as the sizes decrease. This scaling is consistent with that observed in ring-cross and ring-disk structures at two length scales (Figure 2j). The relationship in Equation (1) also applies to 3D structures made of a single material, where the equivalent modulus $\hat{E}$ and density $\hat{\rho}$ simply become the modulus E and density ρ of this material. The scaling agrees well with FEA results for more than ten different 3D structures including the four structures studied here (table, ring, ring-cross, and ring-disk structure), as shown by Figures S4 and S5 (Supporting Information), as well as the experimental results in Figure 2k,l.

Two-floor structures demonstrate that broadband amplitude-frequency behavior can be achieved by mechanically multistable 3D vibrational platforms (**Figure 3**). Figure 3a shows a top-view SEM image and FEA results of three structures in SU8 (10 µm), fabricated using the same process from identical precursors formed at the same time, that are in three stable states. The ribbons on the second floor exhibit three different stable states: 0 downward ribbon (state 1), 1 downward ribbon (state 2), and 2 downward ribbons (state 3). Each of the three structures corresponds to a local minimum in the total strain energy. FEA indicates that a small perturbing force applied at the initial stage of the buckling process can cause the structure to transform from one state to another. By contrast, this perturbing force must be large if applied after 3D assembly. Figure 3b illustrates left-right and up-down resonant modes of the three states, and Figure 3c,d presents the measured amplitude-frequency responses. Resonant frequencies of the left-right mode vary significantly among these cases. State 1 (0 downward ribbon) has the highest resonant frequency at 15.4 kHz. The resonant frequencies of states 2 and 3 are 12.95 and 11.5 kHz, respectively. Therefore, the resonant frequencies of the left-right mode decrease as the number of downward ribbons increases. The up-down mode follows the same trend, although with a comparatively small magnitude. The resonant frequencies of the up-down mode are 18.8, 18.65, and 17.5 kHz, respectively, for states 1, 2, and 3. Figure 3e summarizes the measured resonant frequencies and the values obtained by FEA, with good agreement (discrepancies less than 7%).

The resonant frequencies of each of these states can be continuously tuned by compressive strain. This capability can be combined with the strategies in state transfer to achieve broadband tunability of the resonant frequency in this multistable structure. A process of design optimization of the shape in the 2D precursor illustrates the opportunities. Here, the resonant frequency (f) is first normalized by $\alpha = fL^2\rho^{1/2}E^{-1/2}h^{-1}$ to exclude the influence of the lateral size (L), the thickness (h), and the material properties (E,ρ). Fixing the size, the widths of the ribbon in the x-direction (w_x) and the y-direction (w_y) serve as the two variables to be optimized, as shown in the inset of Figure 3f. The target is to maximize the ratio ($\alpha_{max}/\alpha_{min}$), in which α_{max} and α_{min} represent the maximum and minimum resonant frequencies of the three buckling states as the compressive strain varies in the range of 10%–50%. A design constraint is that the resonant frequency should be tunable in a continuous manner from the minimum to the maximum value without any gap. Only the first-order mode, namely, the left-right mode, is considered. The ratio $\alpha_{max}/\alpha_{min}$ appears as a function of L/w_x and w_y/w_x in Figure 3f. The optimal design

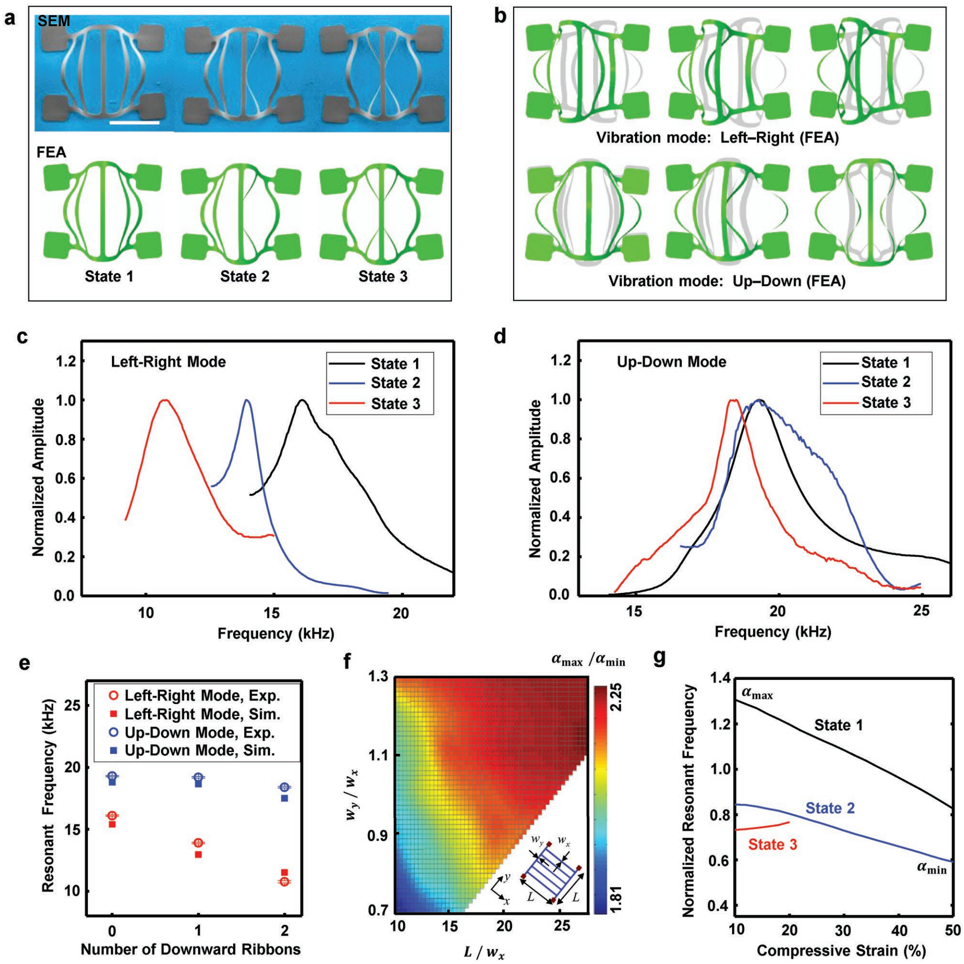

Figure 3. Broadband amplitude-frequency responses achieved in 3D structures with multistable mechanics. a) SEM images and FEA results of three stable states of two-floor 3D structures. Scale bar: 500 µm. b) FEA images of vibrational modes, green: phase 0°, gray: phase 180°, in which the amplitudes are magnified to clearly illustrate the modes. c,d) Measured amplitude-frequency responses of left-right and up-down vibrational modes, respectively. e) Comparison between measured resonant frequencies and simulations. f) Optimization of the operating frequency bandwidth by designing the geometries of the precursor. g) Simulated variations in the normalized resonant frequency as a function of compressive strain for an optimized structure. The normalized resonant frequency can be continuously tuned from 0.59 to 1.31 by changing the compressive strain and shifting the buckled state.

reaches a ratio of $\alpha_{max}/\alpha_{min}$ = 2.25, and in this case, the normalized resonant frequency α can be continually tuned from 0.59 to 1.31 as shown by Figure 3g. Note that only two buckling states (1 and 2) are needed to achieve the tunable resonant frequency band, as the other state (i.e., state 3) does not provide any additional broadening.

A set of complex 3D structures illustrates the diversity of vibrational behavior that can be realized (**Figure 4**). Figure 4a shows SEM images and FEA results of a sixfold rotationally symmetric flower structure (SU8, 10 µm in thickness) and its amplitude-frequency response for the left-right mode. The first resonance corresponds to the vibration of the petal tip. Figure 4b presents an eightfold rotationally symmetric umbrella structure (SU8, 10 µm in thickness). Similar to the flower structure, amplitude-frequency response of the left-right mode exhibits a single peak that corresponds to a global resonance of the structure. Asymmetric geometries are also possible. Figure 4c illustrates a triple-cantilever structure (SU8, 10 µm in thickness) that has cantilever beams with different lengths connected to a triangular membrane. The beam "B1" is the longest, and "B3" is the shortest. Therefore, the resonant frequency of B1 is lowest, and B3 is highest. The resonant frequency of the membrane is higher than that of the beams. Figure S6c (Supporting Information) shows its vibrational modes. The resonance of the beam is localized and largely decoupled from deformations of the membrane. By contrast, the resonance of the membrane leads to global vibration of the entire structure. This example illustrates the ability to decouple local and global resonances in complex 3D vibrational platforms.

Figure 4d presents an asymmetric circular helix (SU8, 10 µm in thickness) that consists of eight ribbons with different lengths. Figure 4d also includes the frequency responses of four ribbons with different lengths. The eighth ribbon is the shortest, and hence its resonant frequency is highest. Various resonances are therefore readily achievable in a single structure. Figure 4e highlights a multilayer cage structure and its

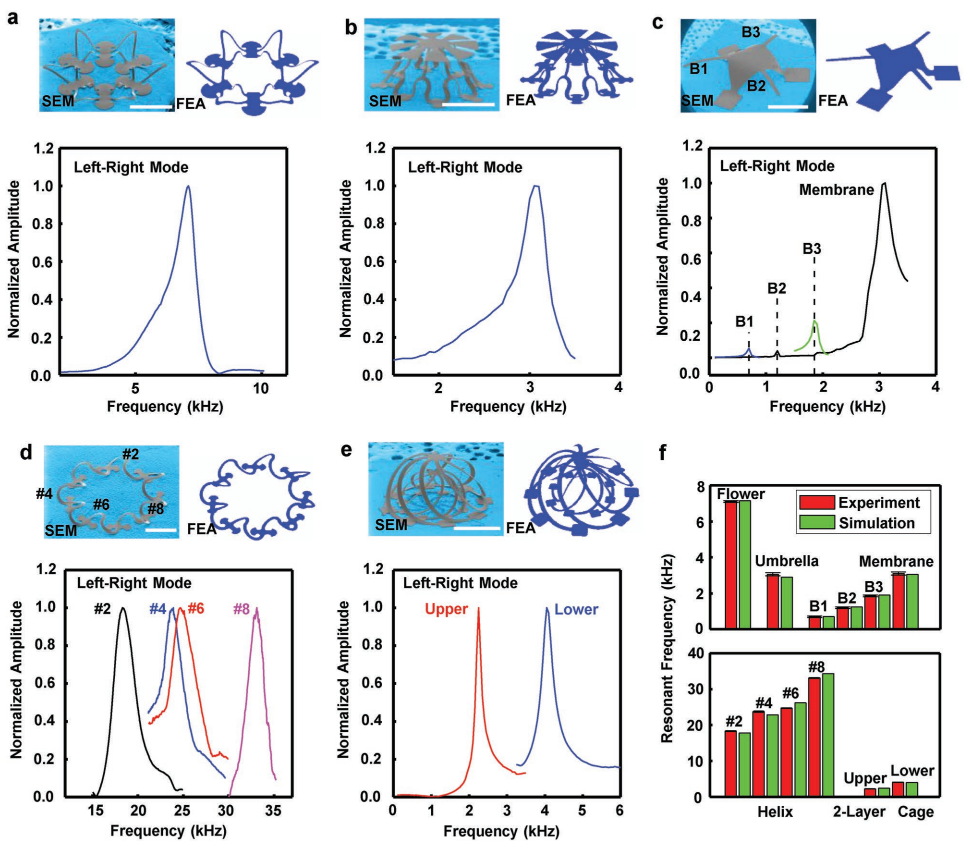

Figure 4. Single-peak and broadband amplitude-frequency responses achieved by structures with diverse 3D geometries. a) SEM images and FEA results for a flower structure (scale bar: 1 mm) and measured amplitude-frequency response for left-right mode. b) SEM images and FEA results of an umbrella structure (scale bar: 1 mm) and measured amplitude-frequency response for the left-right mode. c) SEM images and FEA results of a triple-cantilever structure (scale bar: 2 mm) and measured amplitude-frequency responses of the three beams and central membrane for the left-right mode. d) SEM images and FEA results of a circular helix structure (scale bar: 500 mm) and measured amplitude-frequency responses of the four ribbons with different lengths for the left-right mode. e) SEM images and FEA results of a two-layer cage structure (scale bar: 1 mm) and measured amplitude-frequency responses of the upper and lower floor for the left-right mode. f) Comparison between measured resonant frequencies and simulations.

amplitude-frequency responses. The lateral size of the lower layer (SU8, 7 mm in thickness) is 50% of the upper layer (SU8, 10 μm in thickness), resulting in a higher resonant frequency. Figure 4f shows comparisons between measured resonant frequencies and FEA results, with good agreement (discrepancies less than 7% for all structures).

3. Conclusion

In summary, this paper presents a systematic study of vibrational modes in 3D structures assembled by compressive buckling. These systems provide high levels of versatility in design of vibrational responses, through (1) structural complexity and dimensional scaling enabled by the assembly process, (2) diversity in materials selections, in single or multicomponent layouts, and (3) reversible geometrical tunability enabled by the mechanical elasticity of the substrate. Multistable mechanics and vibrational decoupling of multiple resonant modes represent some consequent strategies for broadband operation, of utility in mechanical resonators, kinetic energy harvesters, and other applications. Rotationally symmetric structures, asymmetric networks, and nested, multilayer layouts can be adapted for various additional mechanovibratory responses. These results suggest that such classes of 3D structures offer potentially important design options that lie outside of the scope of possibilities supported by traditional MEMS technologies.

From a design perspective, the results provide several important considerations and options. (1) Decreasing the lateral dimensions and increasing the stiffnesses of 3D microstructures that consist mainly of ribbons increase their resonant frequencies and therefore improves their detection limits when used for mass sensing. (2) Reversible geometrical deformations of 3D microstructures alter their resonant frequencies in well-defined ways, of relevance for devices that require tunable response. (3) Selection of constituent materials provides a route to meet requirements for operating frequencies in devices that involve a fixed, or a narrow range of in-plane dimensions. (4) Multistable 3D microstructures offer alternative options for broadband frequency operation, of importance for use in mechanical energy harvesters. (5) Multilayer and asymmetric 3D microstructures can serve as ideal platforms for devices that require multiple separated resonant frequencies and modes.

4. Experimental Section

Fabrication of 3D structures in SU8, Si, and SU8/Si followed previously reported procedures.[46–49] Figure S7 (Supporting Information) presents a schematic illustration of the fabrication procedures. Preparation of SU8 3D structures began with spin-casting SU8 on a silicon wafer with a layer of thermally grown silicon dioxide (SiO_2, 800 nm in thickness), followed by a photolithographic procedure to produce 2D precursors. Immersing the wafer in buffered oxide etch (BOE) removed the exposed SiO_2 and slightly etched the SiO_2 underneath the precursors. Spin-casting and photolithography defined a pattern of photoresist (AZ5214E, MicroChemicals) to cover the precursors except their bonding sites. The AZ5214E served as a sacrificial layer to facilitate transformation of precursors into 3D structures, described below. Immersing the wafer in hydrofluoric acid (HF) fully removed the SiO_2 and completed fabrication of SU8 precursors. Transferring the precursors onto a polydimethylsiloxane (PDMS) stamp and then to a sheet of water-soluble tape (polyvinyl alcohol, PVA) prepared samples for compressive buckling on an elastomeric substrate. Exposing a prestretched sheet of silicone elastomer (Dragon Skin, Smooth-on) and the precursors on the PVA tape to UV-induced ozone activated hydroxyl termination to facilitate bonding between the precursors and elastomeric substrate. Attaching the PVA tape on the substrate and baking them in an oven at 70 °C for 9 min yielded strong bonding. Immersion in hot water and then in acetone removed the PVA tape and the AZ5214E sacrificial layer. Releasing the stretched substrate geometrically transformed the 2D precursors into 3D structures.

Preparation of 3D structures of Si began with photolithographic patterning of etching masks (AZ5214E) on a silicon-on insulator (SOI) wafer. Reactive ion etching (RIE) of the exposed regions of the top silicon layer (1.5 µm in thickness) defined the geometry of the 2D Si precursors. Immersion in Nanostrip at 100 °C for 10 min removed the AZ5214E. The remaining steps were identical to those for the SU8 structures.

Preparation of SU8/Si structures combined the steps described above. In particular, the process began with patterning the Si layer of a SOI wafer, followed by spin-casting an adhesive layer (OmniCoat, MicroChem) to improve adhesion between Si and SU8. The remaining steps were identical to those for the SU8 structures.

A 3D-printed testing stage with integrated piezoelectric actuators excited vibrations of 3D structures under test (Figure S8, Supporting Information). Figure S8a (Supporting Information) shows an optical image of the stage and actuators. The latter consisted of a central platform, translational arms, slots for housing actuators, and a base frame. Two piezoelectric chips (Thorlabs, 75 V Piezoelectric Chips. 2.8 µm in stroke) placed in two slots of the stage served as actuators to excite vibrations of 3D structures. A function generator (Keithley 3390) applied sinusoidal voltage on the actuators, thereby exciting vibrations at desired frequencies. A positive driving voltage created expansion in the actuators and associated applied forces on the translational arms, leading to vibration of the central platform. The elastomeric substrate for the 3D structures under test was attached to the central platform by a layer of double-sided tape. Vibration of the platform led to vibrations in the 3D structure. The testing stage can generate vibrations in *X*- and *Y*-directions (parallel to the surface of elastomer substrate). Placing 3D structures on the top surface of an actuator (Figure S8b, Supporting Information) generated vibrations in the *Z*-direction (perpendicular to the surface of elastomer substrate).

A laser measurement system served as the apparatus to investigate the dynamic behavior of 3D structures (Figure S8c, Supporting Information). A focusing lens and mirror delivered a focused laser beam onto a targeted region of a 3D structure under test. The 3D structure and supporting stage were mounted on a mechanical stage capable of translation in *X*-, *Y*-, and *Z*-directions and tilt with respect to *X*- and *Y*-axes. Light scattered from the 3D structures was reflected by a second mirror, collected by a second lens and directed to a photodetector (Thorlabs, DET110) to allow measurement of the intensity. In each measurement the position of the 3D structure was carefully adjusted to ensure that the laser beam focused on the structure and the scattered light was collected by the photodetector. A microscope facilitated the focusing and aligning operations. A pinhole shutter placed in front of the photodetector allowed only a fraction of the scattered laser to be collected by the photodetector.

Vibrations of the 3D structure created fluctuations in the intensity of scattered laser collected by the photodetector, with the same overall time dependence. A lock-in amplifier (SRS 830, Stanford Research Systems) measured the amplitude of fluctuating photocurrent. This system does not, of course, directly determine the vibrational amplitude. In each case, the setups were adjusted such that the amplitude of the photocurrent responded linearly to the amplitude of driving voltage. In this regime of operation, the amplitude of the fluctuating photocurrent is directly proportional to the vibrational amplitude. The amplitude of the photocurrent measured in this way reached a maximum at the resonant frequency.

A Labview program automatically swept the desired range of frequency and recorded data from the lock-in amplifier. At each frequency, the program waited for 4 s before recording data, to ensure stable vibration. 64 data points were recorded at each frequency and the increment of frequency was 50 Hz. All the amplitude-frequency curves presented in this paper were the average among the 64 data points at each frequency.

Supporting Information

Supporting Information is available from the Wiley Online Library or from the author.

Acknowledgements

X.N., H.W., and X.Y. contributed equally to this work. Y.X. acknowleges the support from the Ryan Fellowship and the Northwestern University International Institute for Nanotechnology. Y.H. acknowledges the support from the NSF (Grant Nos. DMR-1121262, CMMI-1300846, and 1534120). Y.H. and J.A.R. acknowledge the support from the NSF (Grant No. CMMI-1400169) and the NIH (Grant No. R01EB019337). Y.Z. acknowledges the support from the National Science Foundation of China (Grant No. 11672152). J.A.R. acknowledges the support from the U.S. Department of Energy, Office of Science, Basic Energy Sciences under Award No. DEFG02-07ER46471.

Received: November 10, 2016
Revised: January 20, 2017
Published online: March 3, 2017

[1] K. Jensen, K. Kim, A. Zettl, *Nat. Nanotechnol.* **2008**, *3*, 533.
[2] M. S. Hanay, S. Kelber, A. K. Naik, D. Chi, E. C. Bullard, E. Colinet, L. Duraffourg, M. L. Roukes, *Nat. Nanotechnol.* **2012**, *7*, 602.
[3] T. P. Burg, M. Godin, S. M. Knudsen, W. Shen, G. Carlson, J. S. Foster, K. Babcock, S. R. Manalis, *Nature* **2007**, *446*, 1066.
[4] I. Etchart, H. Chen, P. Dryden, J. Jundt, C. Harrison, K. Hsu, F. Marty, B. Mercier, *Sens. Actuators, A* **2008**, *141*, 266.
[5] N. Belmiloud, I. Dufour, A. Colin, L. Nicu, *Appl. Phys. Lett.* **2008**, *92*, 041907.
[6] S. Boskovic, J. W. M. Chon, P. Mulvaney, J. E. Sader, *J. Rheol.* **2002**, *46*, 891.
[7] S. Cerimovic, R. Beigelbeck, H. Antlinger, J. Schalko, B. Jakoby, F. Keplinger, *Microsyst. Technol.* **2012**, *18*, 1045.
[8] C. Moraes, C. A. Simmons, Y. Sun, *CSME Bull. SCGM* **2006**, 15.
[9] K. Park, L. J. Millet, N. Kim, H. Li, X. Jin, G. Popescu, N. R. Aluru, K. J. Hsia, R. Bashir, *Proc. Natl. Acad. Sci. USA* **2010**, *107*, 20691.
[10] K. Park, L. Millet, N. Kim, H. Li, K. J. Hsia, N. R. Aluru, R. Bashir, presented at *16th Int. Solid-State Sensors, Actuators and Microsystems Conf.* June **2011**, Beijing.

[11] R. Jagannathan, M. T. A. Saif, *J. Micromech. Microeng.* **2011**, *21*, 054002.
[12] M. Unal, Y. Alapan, H. Jia, A. G. Varga, K. Angelino, M. Aslan, I. Sayin, C. Han, Y. Jiang, Z. Zhang, *Nanobiomedicine* **2014**, *4*, 7173.
[13] P. Christian, M. Dominic, S. Wolfram, M. Florian, M. Yiannos, *J. Micromech. Microeng.* **2009**, *19*, 094004.
[14] P. L. Green, E. Papatheou, N. D. Sims, *J. Intell. Mater. Syst. Struct.* **2013**, *24*, 1494.
[15] G. N. Rameshaiah, J. Pallavi, *Micro Perspectives For Decentralized Energy Supply*, Wiley-VCH, Weinheim, **2015**, p. 170.
[16] I. Dufour, A. Maali, Y. Amarouchene, C. Ayela, B. Caillard, A. Darwiche, M. Guirardel, H. Kellay, E. Lemaire, F. Mathieu, C. Pellet, D. Saya, M. Youssry, L. Nicu, A. Colin, *J. Sens.* **2012**, *2012*, 9.
[17] J. Park, S. Jeong, S. J. Kim, J. Park, *Rev. Sci. Instrum.* **2015**, *86*, 015002.
[18] M. Youssry, N. Belmiloud, B. Caillard, C. Ayela, C. Pellet, I. Dufour, *Sens. Actuators, A* **2011**, *172*, 40.
[19] B. Jakoby, E. Reichel, F. Lucklum, B. Weiss, C. Riesch, F. Keplinger, R. Beigelbeck, W. Hilber, *Mechanics and Model-Based Control of Smart Materials and Structures*, Springer, Berlin **2010**.
[20] H. Cho, M.-F. Yu, A. F. Vakakis, L. A. Bergman, D. M. McFarland, *Nano Lett.* **2010**, *10*, 1793.
[21] S. Lee, C. Chen, V. V. Deshpande, G.-H. Lee, I. Lee, M. Lekas, A. Gondarenko, Y.-J. Yu, K. Shepard, P. Kim, J. Hone, *Appl. Phys. Lett.* **2013**, *102*, 153101.
[22] H. Takahashi, M. Nakayama, T. Shimizu, M. Yamato, T. Okano, *Biomaterials* **2011**, *32*, 8830.
[23] K. Lau, H. Tao, H. Liu, J. Wen, K. Sturgeon, N. Sorfazlian, S. Lazic, J. T. A. Burrows, M. D. Wong, D. Li, S. Deimling, B. Ciruna, I. Scott, C. Simmons, R. M. Henkelman, T. Williams, A.-K. Hadjantonakis, R. Fernandez-Gonzalez, Y. Sun, S. Hopyan, *Nat. Cell Biol.* **2015**, *17*, 569.
[24] P. Campinho, M. Behrndt, J. Ranft, T. Risler, N. Minc, C.-P. Heisenberg, *Nat. Cell Biol.* **2013**, *15*, 1405.
[25] J. Dumais, S. L. Shaw, C. R. Steele, S. R. Long, P. M. Ray, *Int. J. Dev. Biol.* **2003**, *50*, 209.
[26] Z. W. Chen, P. Joli, Z. Q. Feng, *Comput. Methods Biomech. Biomed. Eng.* **2015**, *18*, 1436.
[27] J. A. Weiss, B. N. Maker, S. Govindjee, *Comput. Methods Appl. Mech. Eng.* **1996**, *135*, 107.
[28] G. A. Holzapfel, T. C. Gasser, R. W. Ogden, *J. Elasticity Phys. Sci. Solids* **2000**, *61*, 1.
[29] D. Balzani, D. Brands, A. Klawonn, O. Rheinbach, J. Schröder, *Arch. Appl. Mech.* **2010**, *80*, 479.
[30] Z.-E.-A. Imed, Y. Peng, *J. Micromech. Microeng.* **2009**, *19*, 125004.
[31] J. Olivares, J. Malo, S. González, E. Iborra, I. Izpura, M. Clement, A. Sanz-Hervás, J. L. Sánchez-Rojas, P. Sanz, *MEMS, MOEMS Micromach. II* **2006**, *6186*, 61860K.
[32] W.-M. Zhang, K.-M. Hu, Z.-K. Peng, G. Meng, *Sensors* **2015**, *15*, 26478.
[33] E. T. Filipov, T. Tachi, G. H. Paulino, *Proc. Natl. Acad. Sci. USA* **2015**, *112*, 12321.
[34] E. T. Filipov, G. H. Paulino, T. Tachi, *Proc. R. Soc. A* **2016**, *472*, 1.
[35] Y. Chen, Y. Zhu, X. Chen, Y. Liu, *Trans. ASME J. Appl. Mech.* **2016**, *83*, 041011.
[36] Y. Chen, Y. Liu, Y. Yan, Y. Zhu, X. Chen, *J. Mech. Phys. Solids* **2016**, *95*, 25.
[37] P. Froeter, X. Yu, W. Huang, F. Du, M. Li, I. Chun, S. H. Kim, K. J. Hsia, J. A. Rogers, X. Li, *Nanotechnology* **2013**, *24*, 475301.
[38] W. Huang, S. Koric, X. Yu, K. J. Hsia, X. Li, *Nano Lett.* **2014**, *14*, 6293.
[39] J. U. Lind, T. A. Busbee, A. D. Valentine, F. S. Pasqualini, H. Yuan, M. Yadid, S.-J Park, A. Kotikian, A. P. Nesmith, P. H. Campbell, J. J. Vlassak, J. A. Lewis, K. K. Parker, *Nat. Mater.* **2016**, DOI:10.1038/nmat4782.
[40] K. Malachowski, M. Jamal, Q. Jin, B. Polat, C. J. Morris, D. H. Gracias, *Nano Lett.* **2014**, *14*, 4164.
[41] W. Xi, C. K. Schmidt, S. Sanchez, D. H. Gracias, R. E. Carazo-Salas, S. P. Jackson, O. G. Schmidt, *Nano Lett.* **2014**, *14*, 4197.
[42] D. Yang, B. Mosadegh, A. Ainla, B. Lee, F. Khashai, Z. Suo, K. Bertoldi, G. M. Whitesides, *Adv. Mater.* **2015**, *27*, 6323.
[43] D. Yang, M. S. Verma, J.-H. So, B. Mosadegh, C. Keplinger, B. Lee, F. Khashai, E. Lossner, Z. Suo, G. M. Whitesides, *Adv. Mater. Technol.* **2016**, *1*, 1600055.
[44] S. Babaee, N. Viard, P. Wang, N. X. Fang, K. Bertoldi, *Adv. Mater.* **2016**, *8*, 1631.
[45] J. R. Raney, N. Nadkarni, C. Daraio, D. M. Kochmann, J. A. Lewis, K. Bertoldi, *Proc. Natl. Acad. Sci. USA* **2016**, *113*, 9722.
[46] S. Xu, Z. Yan, K.-I. Jang, W. Huang, H. Fu, J. Kim, Z. Wei, M. Flavin, J. McCracken, R. Wang, A. Badea, Y. Liu, D. Xiao, G. Zhou, J. Lee, H. U. Chung, H. Cheng, W. Ren, A. Banks, X. Li, U. Paik, R. G. Nuzzo, Y. Huang, Y. Zhang, J. A. Rogers, *Science* **2015**, *347*, 154.
[47] Y. Zhang, Z. Yan, K. Nan, D. Xiao, Y. Liu, H. Luan, H. Fu, X. Wang, Q. Yang, J. Wang, W. Ren, H. Si, F. Liu, L. Yang, H. Li, J. Wang, X. Guo, H. Luo, L. Wang, Y. Huang, J. A. Rogers, *Proc. Natl. Acad. Sci. USA* **2015**, *112*, 11757.
[48] Z. Yan, F. Zhang, J. Wang, F. Liu, X. Guo, K. Nan, Q. Lin, M. Gao, D. Xiao, Y. Shi, Y. Qiu, H. Luan, J. H. Kim, Y. Wang, H. Luo, M. Han, Y. Huang, Y. Zhang, J. A. Rogers, *Adv. Funct. Mater.* **2016**, *26*, 2629.
[49] Y. Liu, Z. Yan, Q. Lin, X. Guo, M. Han, K. Nan, K.-C. Hwang, Y. Huang, Y. Zhang, J. A. Rogers, *Adv. Funct. Mater.* **2016**, *26*, 2909.